Splice_sim: a nucleotide-conversion enabled RNA-seq simulation and evaluation framework

Niko Popitsch[1]*#, Tobias Neumann[2,3,4]*, Arndt von Haeseler[4,5], Stefan L. Ameres[1,6]

1 Max Perutz Labs, University of Vienna, Vienna BioCenter, 1030 Vienna, Austria

2 Quantro Therapeutics, 1030 Vienna, Austria

3 Vienna Biocenter PhD Program, a Doctoral School of the University of Vienna and Medical University of Vienna, 1030 Vienna, Austria

4 Center for Integrative Bioinformatics Vienna, Max Perutz Labs, University of Vienna, Medical University of Vienna, 1030 Vienna, Austria

5 Bioinformatics and Computational Biology, Faculty of Computer Science, University of Vienna, 1090 Vienna, Austria

6 Institute of Molecular Biotechnology, IMBA, Vienna BioCenter, 1030 Vienna, Austria

* These authors contributed equally to this work

corresponding author, niko.popitsch@univie.ac.at

Abstract

Nucleotide-conversion (NC) RNA sequencing techniques interrogate chemical RNA modifications in cellular transcripts, but biases in mapping the resulting mismatch-containing reads to reference genomes remain poorly understood. Here, we present *splice_sim*, a splice-aware RNA-seq simulation and evaluation pipeline that introduces user-defined NCs at set frequencies, creates mixture models of converted and unconverted reads and calculates mapping accuracies per genomic annotation. By simulating NC RNA-seq datasets under realistic experimental conditions (including metabolic RNA labelling and RNA bisulfite sequencing), we measured mapping accuracies of state-of-the-art spliced-read mappers for >100,000 mouse and human transcripts and derived strategies to prevent biases in the interpretation of such data.

Keywords

Nucleotide-conversion sequencing; metabolic RNA labelling; SLAMseq; RNA-BS-seq; 3'end sequencing; spliced read mapping; read mapping accuracy

Background

Nucleotide-conversion (NC) RNA sequencing techniques are powerful methods to study post-transcriptional modifications across a wide range of organisms and cell types [1]. In these techniques, RNA is exposed to dedicated nucleotide conversion chemistry and subjected to cDNA library preparation and high-throughput sequencing, ultimately resulting in reads that exhibit zero, one or more specific NCs. Reads are then mapped to a reference sequence and grouped into labelled (one or more NC) and unlabelled (no NC) reads. Grouped read counts are finally combined to quantitative measures of interest and analysed/interpreted to gain novel biological insights.

Several NC RNA-seq protocols that monitor a range of RNA modifications but differ in the type and penetrance of NCs have been introduced recently. These include metabolic RNA labelling techniques with low (1-5%) NC rates that are being used to study the cellular rates of RNA synthesis, processing, translation, and decay. Here, cells are subjected to metabolic RNA labelling with the nucleotide analog 4-thiouridine (4sU). Upon RNA extraction and chemical treatment, 4sU is converted into cytosine or cytosine analogs, allowing to distinguish newly synthesised from pre-existing transcripts due to the presence of T-to-C conversions. The fraction of converted reads (FCR; Table 1) per transcript annotation is, for example, used to estimate half-lives of RNA molecules [2, 3, 4]. In contrast to metabolic RNA sequencing, RNA bisulfite sequencing (RNA-BS-seq) is an example for a NC RNA-seq protocol with very high (>98%) conversion rates. This approach enables the mapping of posttranscriptional cytosine methylation that has been proposed to play a role in RNA regulation, structure, stability, translation and, if mis-regulated, also in disease (progression) [5, 6, 7, 8]. Here, methylated cytosines are protected from being deaminated into uracil upon bisulfite treatment and methylation rates of 5-methylcytosine (m^5C) sites are assessed upon sequencing of cDNA libraries by determining the fraction of unconverted reads at any given cytosine site (metR, methylation rate; Table 1).

Depending on conversion-frequencies, NC RNA-seq datasets are expected to be vulnerable to biases in mapping due to the presence of mismatches that may affect their unique assignment to specific regions in the genome: If, for example, converted reads from a metabolic labelling experiment show considerably lower mapping accuracies than unconverted reads due to increased mismatches to the reference sequence, then resulting FCR values and in consequence derived half-lives would be affected. Accordingly, variations in mapping accuracies for reads with different numbers of m^5C sites may consequently lead to false-negative and false-positive annotation of m^5C sites. Thus, to estimate the reliability of these measures, we need to understand how NCs influence the accuracy of mapping reads to their originating genomic location.

Here, we set out to study mapping accuracies of NC reads, focussing on the evaluation of splice-aware read mappers because NC conversion approaches are often applied to problems that benefit from or require spliced read alignments. Examples include the (relative) quantification of different gene isoforms to investigate alternative splicing mechanisms or intron splicing kinetics [9] (by comparing read counts from (NC converted) unspliced (premature) isoforms with counts from fully spliced (mature) isoforms, FMAT; Table 1). RNA-seq quantification based on spliced alignments was furthermore reported to be more accurate when compared to transcriptome mapping and lightweight quasi-mapping approaches [1, 10]. We do, however, also evaluate the impact of NC on transcript quantification by 3'end mRNA sequencing, an alternative, cost-efficient protocol that does not require spliced read mapping [11].

Measure	Simplified Formula	Applications
FCR: Fraction of converted reads	$\frac{\#converted\_reads}{\#all\_reads}$	e.g., RNA stability measurement (half-life estimation)
metR: Methylation rate	$\frac{\#unconverted\_reads\_at\_site}{\#all\_reads\_at\_site}$	e.g., post-transcriptional RNA methylation
FMAT: Fraction of mature isoform	$\frac{\#mature\_isoform\_reads}{\#all\_reads}$	e.g., RNA splicing kinetics; applied to converted and unconverted reads

Table 1: Exemplary measures based on the comparison (ratio) of different (NC) read groups

Generally, read mapping accuracy is influenced by read length, the number of mismatches to the reference sequence (by NCs and sequencing errors) as well as the general genome mappability of the respective genomic sequence. Genome mappability describes the ability of read mappers to accurately place and align reads of a specific length to respective genomic regions. It is largely determined by the repetitiveness of the genome [12]. Highly repetitive regions account for large shares of eukaryotic genomes and are found in non-coding as well as coding regions (Fig. S1, [13, 14]). Their reduced mappability results in misplaced (false-positive, FP) and missing (false-negative, FN) reads and consequently reduced reliability of biological interpretation derived from respective read alignments.

While mappability of unmodified short reads has been intensely studied in the past [12, 14, 15], much less has been done to address mappability of NC reads. A notable exception is bisulfite sequencing where the bisulfite reaction converts unmethylated cytosine to uracil that is ultimately read as thymine. The high conversion efficiency of this reaction leads to reads with high fractions of C-to-T conversions that are only reliably mappable with specially designed mappers, e.g., Bismark [16], BSMAP [17] or meRanGs [18]. These mappers employ a three-nucleotide letter (3N) alignment strategy: all cytosines in the reads and the reference sequence are converted to thymines and read mapping is based on the remaining three bases

(T, A, G). While this makes 3N mappers insensitive to the number of converted cytosines in the reads, it reduces mappability due to the lower complexity of the mapped sequences and their targets. First approaches to investigate this systematically can be found in Karimzadeh et al. [19], who identified uniquely mappable regions in unconverted and fully bisulfite-converted human and mouse genomes. More recently, Zhang et al. [20], evaluated their HISAT-3N mapper that implements a generalised 3N alignment strategy, allowing arbitrary NCs, on simulated bisulfite and metabolic labelling data. Besides reporting improved mapping accuracies when comparing to other 3N mappers, they also observed an expected increase in multi-mapped reads but overall similar mapping accuracies when comparing 4N and 3N alignments of unmodified reads.

Here, we extend and generalise these findings by comprehensively assessing mapping accuracies of NC reads under different conditions (low to high conversion rates) and their impact on downstream analyses. For this purpose, we developed *splice_sim*, a specialised RNA-seq simulation and evaluation pipeline that (i) simulates short reads with realistic sequencing errors from arbitrary mixes of (partially) spliced and unspliced isoforms per transcript, (ii) introduces arbitrary NCs with a given rate as well as a configurable set of single-nucleotide variations (SNVs) into these reads, and (iii) creates mixed models of converted and unconverted reads. *Splice_sim* then maps simulated reads using a configurable set of mappers and calculates differential alignments between simulated 'truth' and mapper output, enabling a comprehensive evaluation of mapping accuracies under different nucleotide conversion rates.

Using *splice_sim*, we generated deep (100X coverage) simulated metabolic labelling RNA-seq datasets with altering conversion rates (1-10%) for mouse and human transcriptomes and evaluated mapping accuracies of converted and unconverted reads for HISAT-3N [20] and STAR [21], a popular spliced read mapper that does not implement a 3N mapping strategy, for various genomic regions of interest (exons, introns, splice-junctions and whole transcripts). We then evaluated the effects of NC mapping accuracies on decay half-life and isoform mix

reconstruction and applied several strategies to correct/improve those measures using our mapping accuracy scores. As a result, we provide comprehensive transcriptome-wide NC mapping accuracy tables for more than 50k mouse and human transcripts each. We repeated our analysis with simulated RNA-BS-seq data (evaluating HISAT-3N and meRanGs, a specialised bisulfite read mapper based on STAR) and evaluated downstream effects on methylation site calling. Finally, we used *splice-sim* to evaluate different analysis strategies for targeted RNA sequencing strategies, such as mRNA 3'end sequencing, an alternative cost-effective approach for quantifying (NC) mRNA abundances.

Our study demonstrates the negative impact of nucleotide conversion rates on the accuracy to estimate measures with direct biological interpretation and thereby sheds light on the dimension of this problem for real-world experiments. We provide mapping accuracy tables for meaningful biological units of interest (transcripts, exons, introns and splice-junctions) and showcase simple algorithms for improving accuracies in problematic regions or for filtering error prone data sections. Using s*plice_sim*, we identified such regions in numerous members of hallmark gene sets [22], demonstrating their biological relevance (Fig. S1). Finally, we provide users with a simulation and evaluation pipeline that can be used to evaluate existing analysis pipelines/tools or to conduct sophisticated *in silico* experiments that can be performed for any species and transcript annotation of interest.

Results

Splice_sim systematically evaluates the performance of read mappers on NC RNA-seq data.

Using *splice_sim*, we simulated a deep metabolic labelling single-read 100nt dataset (m_big) covering >50k GENCODE (https://www.gencodegenes.org/) annotated canonical mouse (mm10) transcripts. For each transcript we simulated the premature (unspliced) and mature (fully spliced) isoform with a target coverage of ~50X per isoform, i.e. ~100X overall. We simulated three replicates with five different T/C conversion rates (0,1,3,5,10%, typically observed in metabolic RNA-seq time course experiments) each and mapped the simulated data with HISAT-3N and STAR. *Splice_sim* then assessed true-positive (TP), false-negative (FN) and false-positive (FP) read counts for different annotation sets: whole transcripts, exons, introns and splice-junctions. For the latter, we counted donor-overlapping, acceptor-overlapping and spliced reads separately. Details about the counting algorithm are provided in the Supplement, a graphical overview of the analysis workflow is shown in Fig. 1A. Mapping accuracy per annotation was quantified using the F_1 measure (an accuracy measure that incorporates precision and recall into one single score) for mature and premature isoforms separately. As genome mappability has arguably a major impact on NC mapping accuracy and is widely used to filter data, we grouped genomic annotations into three mappability classes (high, medium, low; cf. Methods and Fig. 1B) based on the observed mappability distributions.

First, we analysed over 12 billion mapped reads to quantify the impact of NC on mapping accuracy using STAR and HISAT-3N. As expected, NC and sequencing errors increased false discovery (FDR) and false negative rates (FNR) for both mappers, as read alignment becomes more difficult with increased numbers of mismatches to the originating genomic sequence (Fig. 1C). Simulated T/C nucleotide changes, however, did not strongly affect HISAT-3N data as those were essentially masked out due to the applied 3N mapping approach. We found

residual elevated FP rates with increasing conversion rates in HISAT-3N to be caused by reads (~2%) mapping to the wrong strand (cf. Fig. S2) and corresponding elevated FN rates to be caused by repetitive regions of the same base composition as the introduced base conversions, likely confusing the repeat index during mapping (Fig. S3). Note that absolute FDR/FNR is dominated by genome mappability which is why the relative increase due to additional mismatches is much smaller for low mappability regions. We then assessed mapping accuracies for different genomic features (Fig. 1D). As expected, mapping accuracy decreases with genomic mappability across all categories. Overall, both evaluated mappers showed high accuracies except for features with low mappability where STAR slightly outperformed HISAT-3N. In accordance with our initial analysis, we observed that STAR's performance dropped with increasing conversion rates due to increasing mismatches between reads and reference sequence while HISAT-3N was largely unaffected due to its 3N mapping approach. For both mappers we observed higher mapping precision than recall (Fig. S4) which indicates that FNs are the main factor for reduced accuracies. We then investigated the effect of reduced mapping accuracies on the fraction of converted reads (FCR), an exemplary measure used in downstream analyses to estimate transcript stabilities (Table 1). We compared exonic FCR values (a plot showing intronic and whole-transcript data is in Fig. S5) derived from mapper specific alignments to the true (simulated) FCR which revealed that both mappers indeed have problems reconstructing this measure in the low mappability segment (Fig. 1E). STAR underestimates the real value while the opposite is true for HISAT-3N, although the latter showed less deviations from the true values. The difference to simulated values is dependent on conversion rates, particularly for STAR. We then tried to improve overall FCR reconstruction by selecting FCR values per exon from the mapper with the smallest difference to the simulated value. When combining this 'mosaic' approach with a filtering strategy that removed transcripts for which none of the mappers returned results close to the simulation (see Methods), the overall mean FCR approached the simulated (true) value and omitted only ~1.3k (~8%) of low mappability exons. We concluded that combining STAR

and HISAT-3N in a genomic-location-specific manner can enhance the quantitative analysis of NC datasets particularly for *loci* that suffer from low overall mappability.

Splice_sim instructs mapping approaches in a reduced sequence space.

Emerging RNA sequencing approaches that target only selected transcript features are gaining popularity by their ability to multiplex in a cost-effective manner large sample numbers within one library. 3'end mRNA sequencing [11, 23, 1], for instance, targets not the entire transcript sequence, but only its 3' end (typically the last 200bp) and considers the resulting counts representative for the whole transcript. In addition, the use of oligo(dT) primers for reverse transcription that binds poly-A tails potentially also enriches for any A-rich region in the transcript body resulting in reads that stem from such 'internal priming' events and 'pollute' the overall signal thereby reducing achieved mapping accuracies. To showcase how our tool can be used to select an optimal read mapping strategy in such a scenario, we configured *splice_sim* to evaluate 3'end mapping accuracies and their impact on downstream analyses in a side-by-side comparison with the full transcript sequencing approach. To cover also internal priming events inherent to 3'end sequencing, we considered two possible extremes: (1) clean amplification of the 200bp 3'ends only and (2) simulating reads from the entire transcript in case there is internal priming along the entire transcript ('transcript noise'). In addition, we investigated distinct mapping strategies by mapping to (i) the whole genome, (ii) the transcript sequences and (iii) their 3'end sequences. Finally, in all cases, only reads overlapping 3'end intervals were counted (Fig. S7). When comparing mean genome mappability for 3'end and whole-transcript annotations, we found the former to be generally higher, irrespective if calculated on the genome level or transcriptome level (Fig. S8A). Overall, mappability of transcripts and their 3'ends seems comparable with the most common change being from medium mappable transcripts to high mappable 3' ends and few extreme cases (e.g., high mappability transcripts with low mappability 3'ends), see Fig. S8B.

In line with the higher mappability, our simulated 3'end sequencing data also showed higher mapping accuracies across all conversion rates and mappability classes. When considering FCR estimations, however, full-length sequencing showed the smallest deviation from the simulated FCR, implying that the larger mapping space of the full transcript allows for more robust FCR estimates (Fig. S8C+D). Mapping 3'end data to the transcriptome showed the worst performance with noticeable differences to simulated values already for high and medium mappability genes. Mapping the same data to the genome in an unbiased way performed clearly better and adding 'noise' (i.e., reads from 'internal priming' events) even seemed to have a beneficial effect. We speculate that here both, converted and unconverted FP reads, are mapped at the same ratio as the TP 3'end reads, therefore making the recall of the FCR more robust despite stemming from FP signal. We concluded that the overall mapping performance in a reduced sequence space does not strikingly aggravate mappability issues, however there is a robustness trade-off for biological measures such as FCR. This is best mitigated by using a genome-mapping approach that offers more mapping space to reads that would otherwise potentially falsely be assigned to transcript 3' ends when restricting the mapping space to transcript sequences only.

A mosaic sequence alignment approach enhances the interpretation of metabolic labelling data with implications for RNA stability measurements.

Intrigued by the observed NC-dependent FCR differences, we simulated metabolic labelling pulse-chase data to estimate the effects of reduced NC mapping accuracies on the downstream analysis of RNA decay half-life reconstruction [4, 24]. In a metabolic labelling pulse-chase experiment, cells are typically exposed to a nucleotide analog (e.g., 4-thiouridine) for a considerable time span to ensure a fully labelled RNA population after which the labelling nucleotide analog is washed out and RNA is extracted at multiple consecutive time points, exposed to nucleotide conversion chemistry followed by cDNA library preparation and sequencing. FCR per time point is determined and normalised. A decay model (typically exponential decay is assumed) is fitted to these data and half-lives are derived which are interpreted as a quantification of RNA stability. Accordingly, we configured *splice_sim* to simulate unlabeled/labelled (5% T-to-C conversion rate) RNA ratios over multiple timepoints following a simple exponential decay model for three different decay rates (fast, medium, slow). We included ~2.3k mature transcripts (of which 2150 were included in this analysis after filtering for minimum transcript length>100bp) and their ~17k introns that are expressed in mouse embryonic stem cells (see Supplement). After simulation, read mapping and counting, we calculated FCR per transcript/intron and time point, fitted an exponential decay model (FCR~$e^{t \times -k}$ where *t* is time and *k* is the decay rate constant) to these data and reconstructed half-lives (Fig. 2A+B). Note that estimated half-lives from simulated data are systematically higher than the true value (cf. Fig. 2B). This is because in this analysis, as in a true world scenario, all reads without a found NC were considered to be stemming from ‘new’ (after washing point) RNA, including a considerable number of reads stemming from ‘old’ RNA that have zero conversions just by chance. Although we could have corrected for this in our simulated data (as we know the origin of each individual read), we decided to treat simulated and mapped data the same way to keep them comparable.

289 Although half-life estimation was robust for most transcripts and introns (Fig. 2+S9), we
290 observed a considerable number of outliers with more than 10% difference to simulated half-
291 lives for both mappers in the medium and low mappability segments. Those outliers over- and
292 underestimated simulated half-lives of >120 protein coding genes (Fig. 2C-G). Again, we
293 applied a 'mosaic' approach by choosing FCR values closest to simulated values from
294 mapper-specific data per transcript. This resulted in fewer outliers and smaller differences to
295 simulated half-lives (Fig. 2E). Most outliers (106) were shared, however, a considerable
296 number were found exclusively in HISAT-3N (94) and STAR (39) alignments. The mosaic
297 approach removed 144 outliers while adding only one additional one (Fig. 2F). Interestingly,
298 HISAT-3N produced worse fits to the decay model as supported by lower observed Efron
299 pseudo-R^2 values (Fig. S10; Methods) and consequently also more half-life outliers for this
300 dataset although it showed better overall FCR reconstruction compared to STAR (Fig. 1E).
301 We found comparable numbers of outliers across all three simulated decay rates.
302
303 **Intron filtering improves isoform mix estimates of low mappability transcripts.**
304 Alignment of spliced reads is particularly difficult as it needs to take the possibility of (typically
305 large) gaps due to spliced out introns into account and requires the accurate placement of
306 short (sometimes single nt) sub-sequences of reads (anchors) that span over these gaps [25,
307 10, 26]. This process is expected to be particularly sensitive to additional mismatches
308 introduced by NC. To assess the influence of low-frequency NCs on mapping accuracies of
309 spliced reads, we counted spliced (stemming from mature gene isoforms) and all informative
310 (spliced and donor/acceptor spanning) reads per splice junction (SJ) and calculated fractions
311 of mature isoform reads (FMAT; fraction mature isoform, Table 1) per SJ and transcript, a
312 metric that is typically used in downstream analyses. We observed that differences between
313 mapper-reconstructed and simulated FMAT values increase with decreasing mappability and,
314 for STAR, also with conversion rate (Fig. 3A). Difference to simulated FMAT values correlated
315 negatively with our F_1 values as expected (Fig. S11). When looking closer at the distribution
316 of FMAT values within genes, we observed that transcripts are often a mosaic of high, medium

and low mappability introns (Fig. 3B). We reasoned that FMAT reconstruction of whole transcripts would benefit from filtering introns with low NC mapping accuracies that pollute the overall signal. We filtered introns based on the observed difference to simulated FMAT (see Methods and Fig. S12+13 for examples) and compared filtered with original FMAT values. Intron filtering decreased differences to the true FMAT values and reduced the overall negative correlation with F_1 values (Fig. 3A+S11). Fig. 3C shows that the improvement due to intron filtering is highest if large fractions of introns were omitted and that HISAT-3N profits more than STAR in low mappability regions. Consequently, we observed a clear improvement in FMAT reconstruction for filtered data when plotting value distributions of low mappability transcripts (Fig. 3D). Additionally, we again tried a 'mosaic' approach by choosing the mapper with the most accurate FMAT value per intron which also improved overall estimations and recovered data for more transcripts compared to the intron filtering approach.

A priori knowledge about true splice junctions considerably improves accuracy of spliced read mapping [27]. To confirm this in our data, we repeated our simulations without passing respective gene model information to the read mappers and found a strong increase in FN spliced reads as well as FP SJ overlapping reads and in consequence a strong underestimation of simulated FMAT values respectively large numbers of introns filtered by our approach (Fig. S14). This underlines the importance of feeding accurate information about known and/or suspected splice junctions to splice-aware read mappers but should also motivate *in silico* experiments to learn about the expected readout for the detection of novel splice junctions from RNA-seq data. A further analysis of SJ detection in our main dataset unveiled that HISAT-3N, when compared to STAR, recovered a higher fraction of the (passed) known SJ while at the same time also reporting a higher number of novel SJs which are per definition false-positive in our dataset (Suppl Fig. S15). Notably, we observed increasing false-positive SJs with increasing conversion rates for both mappers.

Low mappability regions are hotspots of false cytosine methylation calls.

Next, we configured *splice_sim* to simulate RNA-BS-seq data which is characterised by high C-to-T conversions rates (98% in our simulation). We used these data to evaluate mapping accuracies of HISAT-3N and meRanGs, a specialised 3N bisulfite RNA-seq read mapper based on STAR. First, we compared overall mapping accuracies in the presence and absence of NCs and found F_1 scores similar to our metabolic labelling dataset. Comparison of the two aligners revealed that meRanGs performed comparably to the general-purpose NC aligner HISAT-3N (Fig. S17A). Interestingly, we observed a slight drop in accuracy for HISAT-3N for the NC dataset but no such drop for meRanGs. We speculate that this drop could be due to the ~2% HISAT-3N reads mapping to the wrong strand (Fig. S2E). Since we stratified our data using genomic mappability scores (umap), we were curious if stratification by methylome mappability scores as presented in [19] led to better predicted mapping accuracy. For this purpose, we compared umap (general mappability) and bismap (methylome mappability) scores and found a high positive correlation (Fig. S17B). We then quantile-normalised bismap scores before creating equally sized mappability class bins for a direct umap to bsmap comparison. Notably, when calculating ΔF_1 values between mappability classes, we did not find any striking difference between the two mappability scores and no clear-cut winner when comparing different mappers, features or mappability classes (Fig. S17C+D). We therefore conducted our analysis using the same (umap-based) genome mappability scores as for the metabolic labelling analysis.

We then set out to measure the effects of mismapped NC reads on calling m^5C sites in a realistic dataset. For this, we spiked a published set of mESC m^5C sites with methylation rates (per site) ranging from 20 to 100% into a *splice_sim* dataset with 1,910 overlapping transcripts and measured how many of them could be recalled (TP), how many were missed (FN) and how many false-positive (FP) calls we would get (see Supplement for a detailed description of this analysis). Simulated and true methylation rates correlated well and overall most m^5C sites were re-called in both mapper-derived datasets (4,811/4,831=99.6%, Fig. 4A+B). Both

mappers did, however, produce a considerable amount of FP and few FN m^5C calls, mainly in low mappability regions of protein coding genes (Fig. 4C-E). When inspecting the data, we found that FP and FN m^5C sites were mainly a result of incomplete (simulated) bisulfite conversion (i.e., not all reads contained a C-to-T NC at a true m^5C site) and missing FN reads in low mappability regions (Fig. S18), in line with reported experimental artifacts of the BS-seq protocol [28, 29, 30, 31].

False positives were called with methylation rates over the whole range (20-100%) which makes such calls not straightforward to filter. Although advanced filtering approaches (e.g., by *in silico* folding of transcripts and checking for the base-pairing status of potential m^5C sites [6, 32]), would likely reduce false calls, our analysis clearly shows that regions of low genome mappability are hotspots of false m^5C calls and should be handled with particular care.

Genome-specific features impact NC RNA-seq data analysis in different species.

Finally, we repeated our analysis with human data (GRCh38, canonical Ensembl genes) using the same configuration parameters as for the mouse data experiments for comparison and reference (Supplementary Table S2). Note that when comparing genome mappability distributions between our selected human and mouse annotations, we found slightly but significantly increased mappability for mouse annotations and more human transcripts in the medium mappability category (Fig. S19). We found, however, also less low mappability transcripts in the human annotations. Human exon/intron annotations were slightly shorter/longer respectively when compared to mouse annotations. Overall, the human data showed very similar results when compared to our mouse datasets with differences possibly explained by the abovementioned difference in mappability distributions.

Discussion

We presented *splice_sim*, a versatile RNA-seq simulation and evaluation framework, and used it for a comprehensive analysis of annotation-based mapping accuracies of regular as well as NC reads that focused on potential effects on downstream analyses. Overall, our analysis revealed that mapping accuracies with and without NC are high ($F_1 > 0.98$) for all considered mappers when considering annotations with high/medium genome mappability but substantially lower ($F_1 < 0.55$) for low mappability ones, a considerable fraction that includes protein coding as well as regulatory RNAs of biological importance (Fig. S1, [12]). Particularly in regions with low genome mappability we observed considerable differences in mapping accuracies among groups of unmodified and NC reads that consequently lead to increased error rates in measures based on the comparison of such read groups (e.g., FCR). Other than for many metrics derived from regular RNA-seq data (e.g., relative abundances), NC mapping biases do not cancel out and we demonstrate that they can lead to wrong estimates of downstream measures (transcript half-lives or isoform estimates) which in turn affect biological implications/interpretations.

Our result tables for mouse and human metabolic labelling and RNA-BS-seq data, including raw counts, performance measures and categorical data, are built on GENCODE annotations and published alongside this manuscript. A summary plot of these tables is provided in Fig. S26: For each transcript, we calculated which of the evaluated mappers showed the best performance with regard to general mapping accuracy, FCR and FMAT reconstruction, reporting both mappers if we observed only small differences and none if we considered the differences to the true values too large for a useful analysis. We demonstrate how our results can guide data cleaning and analysis strategies: using simple approaches such as best mapper selection (e.g., in a ‘mosaic’ approach) or filtering of identified problematic introns, we were able to improve overall accuracy of derived measures and thereby biological interpretability. The demonstrated accuracy gains due to ‘mosaic’ filtering demonstrate that

the evaluated mappers differ to some extent in the made mapping errors due to their differing alignment algorithms/approaches and overall our evaluation does not render one of them superior to the others. In practice, a 'mosaic' filtering strategy, however, requires the generation of (at least) two alignments per dataset thereby increasing analysis costs. As an alternative, intron filtering can be used to improve FMAT predictions as demonstrated. Our datasets furthermore provide information about which transcripts cannot be analysed with respect to what measures reliably with short read data and should be handled with care or omitted from analysis.

We provide fine-grained precompiled result sets for all annotated transcripts of the GENCODE annotation that is useful for benchmarking mappers on NC data sets. Users can directly look up how a given mapping tool will perform on their genomic feature of interest and take countermeasures to mitigate bad estimates from problematic regions. Users are also encouraged to apply our software and analysis scripts to calculate mapping accuracy data for alternative model organisms and annotation sets and devise new data cleaning and filtering strategies. While our study considered the entirety of the (theoretically) expressed mouse and human transcriptomes, *splice_sim* is applicable to arbitrary genomes and genomic annotations, thereby also allowing to study NC mapping accuracies in non-coding regions of the genome.

Splice_sim can also be used to measure the potential impact of sequencing protocols and analysis pipelines on read mapping accuracies and downstream measures, thereby helping to develop best practices for experiments and data analysis. By comparing datasets with and without passing known splice sites to the read mapper we could, for example, confirm the large impact of this knowledge on spliced read mapping accuracy. We also demonstrated that 3'end sequencing is a valid alternative to whole-transcript sequencing, which has advantages for certain applications, such as FCR estimation, and showed that it is beneficial to map 3'end reads to the whole genome to get most accurate FCR estimations. Finally, we demonstrated

453 that low mappability regions are hotspots of false m^5C calls that are not straightforward to filter
454 based on measured methylation rates. Besides experimental optimizations of RNA-BS-seq
455 protocols, *splice-sim* can thus help to establish accurate and reproducible sets of true m^5C
456 sites in mammalian transcriptomes which were reported with large variation (ranging from
457 <100 to >10k sites) in current literature [7].
458
459 **Related work.** *Splice_sim* distinguishes itself from previous RNA-seq simulators by its ability
460 to simulate mixtures of regular and NC reads and its evaluation module that provides users
461 with detailed mapping accuracy assessments and additional resources (such as read
462 highlighting and BAM files containing misaligned reads) that are useful for subsequent
463 processing/analyses [33, 34]. *Splice_sim* supports arbitrarily complex isoform mixes,
464 comparable to Polyester [35] and uses ART [36] for the actual simulation of (unmodified) high-
465 throughput sequencing reads, but this module could easily be replaced by alternative RNA-
466 seq simulators (e.g., Camparee [37], BEERS [38], or RSEM [39]). Notably, splice_*sim*
467 quantifies mapping accuracies for entities of direct biological interpretation (e.g., exons and
468 introns) instead of general genomic regions as most previous work on genome mappability to
469 which our work is complementary [40, 19, 15].
470
471 **Limitations.** There are some limitations to our chosen approach for estimating mapping
472 accuracies: First, our method is based on simulations as it is obviously unfeasible to iterate all
473 possible NC reads which could lead to biases due to stochastic effects. We are, however,
474 confident that stochastic effects would be rather small based on our analysis of three replicates
475 that showed very high correlation (Fig. S22).
476 Second, for our main dataset (***m_big***) we configured *splice_sim* to simulate one transcript for
477 each annotated mouse gene with similar read coverage which also means that reads from all
478 transcripts can be mismapped and potentially contribute to false-positive counts. Our results
479 should thus be interpreted as worst-case scenarios in this regard, and we encourage users to
480 repeat our analysis with a configuration that better reflects transcript expression levels in their

cell-type of interest (e.g., estimated from standard RNA-seq data) to avoid this bias. Comparing our data to a smaller dataset containing only transcripts that are actively described in mESC, however, showed high correlation and only small differences that could be attributed to inflated FP counts (Fig. S23). We also investigated what fraction of FP reads change their labelling status (i.e., from labelled to unlabelled or *vice versa*) due to misalignment that introduces/masks NCs but found this to be a minor problem (Fig. S24).

Third, *splice_sim* is currently based on single-end reads only, a configuration that is widely considered as a cost-effective option for standard and NC RNA-seq experiments. Nevertheless, paired-end data would have two central advantages in the discussed experimental settings: first, it would arguably improve overall mappability as both mates would contribute to overall (fragment) mappability. Second, overlapping mates could be used to correct for sequencing errors in the overlapping regions [41]. We therefore plan to extend our software to support such scenarios in the future.

Conclusions

Our study demonstrates how minor differences in mapping accuracy between regular and nucleotide-converted reads may cause considerable numbers of outliers and false calls in downstream measures with direct biological interpretation, such as RNA stabilities or post-transcriptional methylation site calls. We provide simulated datasets and analyses for understanding the dimension of this problem and conclude that these biases should not be ignored when analysing experimental data. Our *splice_sim* simulation and evaluation pipeline and the datasets published alongside this manuscript may be used for data filtering and/or correction as demonstrated, thereby improving overall data accuracy and reliability of derived biological interpretations.

Methods

Splice_sim is implemented by a set of Python and R scripts that are orchestrated by nextflow pipelines [42]. The complete software stack is bundled in a Docker container to increase reproducibility and usability. A detailed description of *splice_sim* is provided in the Supplement. Briefly, it simulates short reads with realistic sequencing errors for a set of configured transcript ids and isoforms and injects NCs with given conversion rates and configurable sets of SNVs with given variant allele frequencies (VAF). For our main evaluation dataset (***m_big***), we simulated 1:1 ratios of premature (unspliced) and mature (fully spliced) isoforms for >50k mm10 (GRCm38) transcripts with five different conversion rates (0, 1, 3, 5, 10%). We simulated three replicates and mapped the reads with STAR and HISAT-3N. Mapped reads were classified as true positive (TP), false positive (FP) or false-negative (FN) with respect to given genomic features of interest (exons, introns, full transcripts and splice junctions) by comparing to the simulated data (see Supplement for a detailed description of this procedure). Resulting count tables were grouped by read mapper, conversion rate, annotation feature id, originating isoform, reads with at least 1/at least 2 NCs and reads with at least 1/at least 2 simulated sequencing errors. Data was annotated with additional meta-data (e.g., GENCODE gene types) as required and analysed in RStudio v2022.02.1. For estimating genome mappability per feature, we downloaded umap mm10/hg38 single-read k24 tracks from https://bismap.hoffmanlab.org and calculated mean values over annotation feature intervals. Features were then classified into three mappability categories: high (mean value>0.9), low (<0.2) and medium.

Mapping performance per annotation (transcript, exon, intron, splice-junction) was measured by precision ($\frac{TP}{TP+FP}$), recall ($\frac{TP}{TP+FN}$) and accuracy using the F_1-measure:$F_1 = 2 \times \frac{precision \times recall}{precision + recall}$ = $\frac{2 \times TP}{2 \times TP + FP + FN}$. Fraction of converted reads per annotation was defined as the ratio between NC containing reads and all reads, $FCR = \frac{\#converted-reads}{\#all-reads}$. All reads with at least one NC were

considered converted. Fraction of mature isoform per transcript was calculated as $FMAT = \frac{\#mature-isoform-reads}{\#mature-isoform-reads+\#premature-isoform-reads} = \frac{\Sigma\ \#spl-reads}{\Sigma\ \#spl-reads + \Sigma\ \#don-reads + \Sigma\ \#acc-reads}$ where *spl*, *acc* and *don* are intron splicing, donor overlapping and acceptor overlapping reads respectively. Given the configured 1:1 ratio between mature and premature isoforms, we expected a theoretical FMAT value of ⅓ and recovered a mean value of 0.334 from our simulated data (cf. Fig. 3D). Intron filtering per transcript was implemented as follows: we first sorted introns by decreasing FMAT difference to the simulated data and consecutively filtered introns with a difference greater than 10% until no more such introns were available or until removal of the next intron would lead to less than 100 remaining informative (spl+don+acc) reads for this transcript.

For the RNA decay experiments, we simulated mature (for transcript decay rates) and premature (for intron decay rates) isoforms for six timepoints with arbitrary units and 5% T/C conversion rate. The fraction of labelled and unlabelled RNA per time point was configured in a way that the resulting FCR values follow a simple exponential decay model $FCR \sim e^{t \times -k}$ where *t* is time and *k* is the decay rate constant. We simulated data for ~2.3k transcripts with three randomly assigned decay rates (fast/k=0.15, moderate/k=0.1, slow/k=0.05), mapped the reads, annotated T-to-C conversions in the BAM files and extracted reads with at least one T-to-C conversion to new BAM files. We then counted reads per genomic annotation with featureCounts [43] for complete and T-to-C-only alignments, calculated FCR per transcript and intron and fitted the data to the exponential model in R. A more detailed description of this procedure is provided in the Supplement. Resulting half-life estimates were compared to the theoretical and simulation-derived values and we compared goodness-of-fit between mappers by Efron's pseudo-R^2 values that were calculated as $1 - \frac{rss}{tss}$ where *rss* is the sum of the squared model residuals and *tss* is the total variability in the dependent variable (Fig. S10).

For the human dataset (**h_big**), we used the same configuration as for **m_big** and simulated data for all GENCODE v39 (GRCh38) transcripts annotated with the Ensembl canonical annotation tag.

For the RNA-BS-seq analysis, we simulated a dataset (**m_big_bs**) containing the same transcripts as **m_big** and 98% C-to-T conversions. For measuring m^5C calling accuracy, we simulated a smaller dataset (**m_small_bs**) with 1910 transcripts that overlap with a set of published methylated m^5C sites called from mESC total polyA RNA-seq data (https://pubmed.ncbi.nlm.nih.gov/28077169, GEO project GSE83432 [32]). Published m^5C sites were spiked into the dataset with given methylation rates, called with meRanCall [18] and compared to the truth set. A more detailed description of this analysis is provided in the Supplement.

For the 3'end analysis, we used the comprehensive full-length transcript dataset (**m_big**) as reference and simulated several 3' end datasets, taking the last 200nt ranging from the transcript 3' ends with different noise levels (see Fig. S7). We then calculated count tables for all scenarios and benchmarked them against the full-length reference set for mapping accuracy and FCR estimation. Applying 3'end sequencing for FMAT estimation was omitted as only few evaluated 200nt 3' ends span a splice-junction. A more detailed description of the 3'end simulation routine is provided in the Supplement.

Note that we also evaluated the effect of mapping quality filtering (as often seen in bioinformatics analysis pipelines) on estimated mapping accuracies and observed a strong decrease in the low mappability segment as expected as filtered reads are treated as FN by our pipeline (Fig. S25). In high/medium mappability segments we observed small but noticeable accuracy decreases. Note that *splice_sim* is by default returning counts for unfiltered and mapping quality (MQ>20) filtered alignments.

Declarations

Ethics approval and consent to participate

Not applicable.

Consent for publication

Not applicable.

Availability of data and materials

The source code of *splice_sim* is available on Github at https://github.com/popitsch/splice_sim under the GPL-3.0 license and the corresponding execution environment is wrapped in a Docker image available at https://hub.docker.com/repository/docker/tobneu/splice_sim. Count tables and result files of all simulated datasets are available at doi:10.5281/zenodo.7704159. We have also deposited the full m_small dataset, including all output from the *splice_sim* pipeline for reference. The full pipeline output for all other datasets is available from the authors upon request.

Competing interests

Tobias Neumann is an employee at QUANTRO Therapeutics. Stefan L. Ameres is a co-founder, scientific advisor and member of the board of QUANTRO Therapeutics. All other authors declare they have no competing interests.

Funding

This research was supported by the European Research Council (ERC-CoG-866166) and the Austrian Science Fund FWF (SFB F-8002) to S.L.A.

Authors' contributions

NP and TN developed *splice_sim* and conducted the computational experiments and analyses. AvH and SLA provided essential feedback and guidance on method development, biological background, and applications. NP and TN wrote the manuscript with input from all authors. All authors have read and approved the final manuscript.

Acknowledgements

The authors thank Daehwan Kim and Yun Zhang for support with HISAT-3N. The computational results presented were obtained using the CLIP cluster (https://clip.science).

References

[1] R. Stark, M. Grzelak and J. Hadfield, “RNA sequencing: the teenage years,” *Nature Reviews Genetics,* vol. 20, p. 631–656, July 2019.

[2] V. A. Herzog, B. Reichholf, T. Neumann, P. Rescheneder, P. Bhat, T. R. Burkard, W. Wlotzka, A. von Haeseler, J. Zuber and S. L. Ameres, “Thiol-linked alkylation of RNA to assess expression dynamics,” *Nature Methods,* vol. 14, p. 1198–1204, September 2017.

[3] L. Kiefer, J. A. Schofield and M. D. Simon, “Expanding the Nucleoside Recoding Toolkit: Revealing RNA Population Dynamics with 6-Thioguanosine.,” *Journal of the American Chemical Society,* vol. 140, no. 44, p. 14567–14570, November 2018.

[4] A. Lusser, C. Gasser, L. Trixl, P. Piatti, I. Delazer, D. Rieder, J. Bashin, C. Riml, T. Amort and R. Micura, “Thiouridine-to-Cytidine Conversion Sequencing (TUC-Seq) to Measure mRNA Transcription and Degradation Rates,” in *Methods in Molecular Biology*, vol. 2062, Springer New York, 2020, p. 191–211.

[5] S. Edelheit, S. Schwartz, M. R. Mumbach, O. Wurtzel and R. Sorek, “Transcriptome-Wide Mapping of 5-methylcytidine RNA Modifications in Bacteria, Archaea, and Yeast Reveals m5C within Archaeal mRNAs,” *PLoS Genetics,* vol. 9, p. e1003602, June 2013.

[6] T. Huang, W. Chen, J. Liu, N. Gu and R. Zhang, “Genome-wide identification of mRNA 5-methylcytosine in mammals,” *Nature Structural & Molecular Biology,* vol. 26, p. 380–388, May 2019.

[7] Z. Johnson, X. Xu, C. Pacholec and H. Xie, “Systematic evaluation of parameters in RNA bisulfite sequencing data generation and analysis,” *NAR Genomics and Bioinformatics,* vol. 4, March 2022.

[8] S.-Y. Chen, K.-L. Chen, L.-Y. Ding, C.-H. Yu, H.-Y. Wu, Y.-Y. Chou, C.-J. Chang, C.-H. Chang, Y.-N. Wu, S.-R. Wu, Y.-C. Hou, C.-T. Lee, P.-C. Chen, Y.-S. Shan and P.-H. Huang, “RNA bisulfite sequencing reveals NSUN2-mediated suppression of epithelial differentiation in pancreatic cancer,” *Oncogene,* vol. 41, p. 3162–3176, May 2022.

[9] L. Wachutka, L. Caizzi, J. Gagneur and P. Cramer, “Global donor and acceptor splicing site kinetics in human cells,” *eLife,* vol. 8, April 2019.

[10] A. Srivastava, L. Malik, H. Sarkar, M. Zakeri, F. Almodaresi, C. Soneson, M. I. Love, C. Kingsford and R. Patro, “Alignment and mapping methodology influence transcript abundance estimation,” *Genome Biology,* vol. 21, September 2020.

[11] P. Moll, M. Ante, A. Seitz and T. Reda, “QuantSeq 3′ mRNA sequencing for RNA quantification,” *Nature Methods,* vol. 11, p. i–iii, November 2014.

[12] R. Koehler, H. Issac, N. Cloonan and S. M. Grimmond, “The uniqueome: a mappability resource for short-tag sequencing,” *Bioinformatics,* vol. 27, p. 272–274, January 2011.

[13] H. Innan and F. Kondrashov, “The evolution of gene duplications: classifying and distinguishing between models,” *Nature Reviews Genetics,* vol. 11, p. 97–108, January 2010.

[14] T. Derrien, J. Estellé, S. M. Sola, D. G. Knowles, E. Raineri, R. Guigó and P. Ribeca, “Fast Computation and Applications of Genome Mappability,” *PLoS ONE,* vol. 7, p. e30377, January 2012.

[15] C. Pockrandt, M. Alzamel, C. S. Iliopoulos and K. Reinert, “GenMap: ultra-fast computation of genome mappability,” *Bioinformatics,* vol. 36, p. 3687–3692, April 2020.

[16] F. Krueger and S. R. Andrews, “Bismark: a flexible aligner and methylation caller for Bisulfite-Seq applications,” *Bioinformatics,* vol. 27, p. 1571–1572, April 2011.

[17] Y. Xi and W. Li, “BSMAP: whole genome bisulfite sequence MAPping program,” *BMC Bioinformatics,* vol. 10, July 2009.

[18] D. Rieder, T. Amort, E. Kugler, A. Lusser and Z. Trajanoski, “meRanTK: methylated RNA analysis ToolKit,” *Bioinformatics,* vol. 32, p. 782–785, November 2015.

[19] M. Karimzadeh, C. Ernst, A. Kundaje and M. M. Hoffman, “Umap and Bismap: quantifying genome and methylome mappability,” *Nucleic Acids Research,* August 2018.

[20] Y. Zhang, C. Park, C. Bennett, M. Thornton and D. Kim, “Rapid and accurate alignment of nucleotide conversion sequencing reads with HISAT-3N,” *Genome Research,* vol. 31, p. 1290–1295, June 2021.

[21] A. Dobin, C. A. Davis, F. Schlesinger, J. Drenkow, C. Zaleski, S. Jha, P. Batut, M. Chaisson and T. R. Gingeras, “STAR: ultrafast universal RNA-seq aligner,” *Bioinformatics,* vol. 29, p. 15–21, October 2012.

[22] A. Liberzon, C. Birger, H. Thorvaldsdóttir, M. Ghandi, J. P. Mesirov and P. Tamayo, “The Molecular Signatures Database Hallmark Gene Set Collection,” *Cell Systems,* vol. 1, p. 417–425, December 2015.

[23] M. Muhar, A. Ebert, T. Neumann, C. Umkehrer, J. Jude, C. Wieshofer, P. Rescheneder, J. J. Lipp, V. A. Herzog, B. Reichholf, D. A. Cisneros, T. Hoffmann, M. F. Schlapansky, P. Bhat, A. von Haeseler, T. Köcher, A. C. Obenauf, J. Popow, S. L. Ameres and J. Zuber, “SLAM-seq defines direct gene-regulatory functions of the BRD4-MYC axis,” *Science,* vol. 360, p. 800–805, May 2018.

[24] V. Agarwal and D. R. Kelley, “The genetic and biochemical determinants of mRNA degradation rates in mammals,” *Genome Biology,* vol. 23, November 2022.

[25] M. Alser, J. Rotman, D. Deshpande, K. Taraszka, H. Shi, P. I. Baykal, H. T. Yang, V. Xue, S. Knyazev, B. D. Singer, B. Balliu, D. Koslicki, P. Skums, A. Zelikovsky, C. Alkan, O. Mutlu and S. Mangul, “Technology dictates algorithms: recent developments in read alignment,” *Genome Biology,* vol. 22, August 2021.

[26] G. Baruzzo, K. E. Hayer, E. J. Kim, B. D. Camillo, G. A. FitzGerald and G. R. Grant, "Simulation-based comprehensive benchmarking of RNA-seq aligners," *Nature Methods,* vol. 14, p. 135–139, December 2016.

[27] P. G. Engström, T. Steijger, B. Sipos, G. R. Grant, A. Kahles, G. Rätsch, N. Goldman, T. J. Hubbard, J. Harrow, R. Guigó, P. Bertone and R. G. A. S. P. Consortium, "Systematic evaluation of spliced alignment programs for RNA-seq data.," *Nature methods,* vol. 10, no. 12, p. 1185–1191, December 2013.

[28] S. M. Huber, P. van Delft, L. Mendil, M. Bachman, K. Smollett, F. Werner, E. A. Miska and S. Balasubramanian, "Formation and abundance of 5-hydroxymethylcytosine in RNA.," *Chembiochem : a European journal of chemical biology,* vol. 16, no. 5, p. 752–755, March 2015.

[29] C. Legrand, F. Tuorto, M. Hartmann, R. Liebers, D. Jacob, M. Helm and F. Lyko, "Statistically robust methylation calling for whole-transcriptome bisulfite sequencing reveals distinct methylation patterns for mouse RNAs.," *Genome research,* vol. 27, no. 9, p. 1589–1596, September 2017.

[30] X. Yang, M. Liu, M. Li, S. Zhang, H. Hiju, J. Sun, Z. Mao, M. Zheng and B. Feng, "Epigenetic modulations of noncoding RNA: a novel dimension of Cancer biology.," *Molecular cancer,* vol. 19, no. 1, p. 64, March 2020.

[31] L. Shen, Z. Liang, C. E. Wong and H. Yu, "Messenger RNA Modifications in Plants.," *Trends in plant science,* vol. 24, no. 4, p. 328–341, April 2019.

[32] T. Amort, D. Rieder, A. Wille, D. Khokhlova-Cubberley, C. Riml, L. Trixl, X.-Y. Jia, R. Micura and A. Lusser, "Distinct 5-methylcytosine profiles in poly(A) RNA from mouse embryonic stem cells and brain," *Genome Biology,* vol. 18, January 2017.

[33] M. Zhao, D. Liu and H. Qu, "Systematic review of next-generation sequencing simulators: computational tools, features and perspectives," *Briefings in Functional Genomics,* p. elw012, April 2016.

715 [34] M. Escalona, S. Rocha and D. Posada, “A comparison of tools for the simulation of
716 genomic next-generation sequencing data,” *Nature Reviews Genetics,* vol. 17, p. 459–469,
717 June 2016.
718 [35] A. C. Frazee, A. E. Jaffe, B. Langmead and J. T. Leek, “Polyester: simulating RNA-seq
719 datasets with differential transcript expression,” *Bioinformatics,* vol. 31, p. 2778–2784, April
720 2015.
721 [36] W. Huang, L. Li, J. R. Myers and G. T. Marth, “ART: a next-generation sequencing read
722 simulator,” *Bioinformatics,* vol. 28, p. 593–594, December 2011.
723 [37] N. F. Lahens, T. G. Brooks, D. Sarantopoulou, S. Nayak, C. Lawrence, A. Mrčela, A.
724 Srinivasan, J. Schug, J. B. Hogenesch, Y. Barash and G. R. Grant, “CAMPAREE: a robust
725 and configurable RNA expression simulator,” *BMC Genomics,* vol. 22, September 2021.
726 [38] G. R. Grant, M. H. Farkas, A. D. Pizarro, N. F. Lahens, J. Schug, B. P. Brunk, C. J.
727 Stoeckert, J. B. Hogenesch and E. A. Pierce, “Comparative analysis of RNA-Seq alignment
728 algorithms and the RNA-Seq unified mapper (RUM).,” *Bioinformatics (Oxford, England),* vol.
729 27, no. 18, p. 2518–2528, September 2011.
730 [39] B. Li and C. N. Dewey, “RSEM: accurate transcript quantification from RNA-Seq data
731 with or without a reference genome,” *BMC Bioinformatics,* vol. 12, August 2011.
732 [40] H. Lee and M. C. Schatz, “Genomic dark matter: the reliability of short read mapping
733 illustrated by the genome mappability score.,” *Bioinformatics (Oxford, England),* vol. 28, no.
734 16, p. 2097–2105, August 2012.
735 [41] J. M. Gaspar, “NGmerge: merging paired-end reads via novel empirically-derived models
736 of sequencing errors,” *BMC Bioinformatics,* vol. 19, December 2018.
737 [42] P. D. Tommaso, M. Chatzou, E. W. Floden, P. P. Barja, E. Palumbo and C. Notredame,
738 “Nextflow enables reproducible computational workflows,” *Nature Biotechnology,* vol. 35, p.
739 316–319, April 2017.
740 [43] Y. Liao, G. K. Smyth and W. Shi, “featureCounts: an efficient general purpose program
741 for assigning sequence reads to genomic features,” *Bioinformatics,* vol. 30, p. 923–930,
742 November 2013.

Figure legends

Figure 1: Analysis workflow and NC mapping accuracies for simulated mouse metabolic labelling data. **A** Analysis workflow overview: briefly, we simulated short reads with realistic sequencing error (red X) for premature and mature isoforms, calculated truth alignments and injected nucleotide conversions with configured conversion rates. Simulated reads were mapped by the evaluated read mappers and resulting alignments were compared to the simulated data. Finally, grouped count tables with true positive (TP), false positive (FP) and false negative (FN) counts per annotation of interest (tx: transcripts, fx: exons + introns, sj: splice junctions) were created and analysed. **B** Numbers of annotations with high (>0.9), medium and low (<0.2) mean genome mappability. **C** Changes of false discovery (FDR=FP/(TP+FP) and false negative (FNR=FN/(TP+FN)) rates by number of mismatches per read compared to reads without mismatches, stratified by mappability and type of mismatch (either simulated NC or random sequencing errors). The plots show median FDR/FNR and interquartile regions (shaded areas) across three **m_big** replicates for STAR (green) and HISAT-3N (orange) alignments. This analysis included ~12B reads originating from premature isoforms and their classification (TP, FP, FN) with respect to whole-transcript annotations. **D** Median F_1 measure per mapper and originating isoform (pre: premature, mat: mature) for different genomic annotations (tx: whole transcript), stratified by mappability. **E** Mean difference to simulated, exonic FCR (fraction of converted reads) per mapper and for a 'mosaic' approach where the mapper with the smallest difference to the simulated value was chosen. The mosaic approach reduces differences to simulated values and when removing exons where none of the two mappers showed good results, reconstruction is nearly perfect (‘mosaic filtered’, see main text). Note that a corresponding plot for human data is provided in Fig. S6 for comparison.

Figure 2: Effect of NC on transcript half-life reconstruction (corresponding plot for introns in Fig. S9). **A** Normalised, mature transcript FCR per time point (arbitrary units) for true,

simulated, and mapped data. The truth data models an idealised exponential decay curve for three randomly assigned decay rates (violet: fast/k=0.15, brown: moderate/k=0.1, magenta: slow/k=0.05). FCR for simulated and mapper-specific alignments was estimated as explained in Methods. The mosaic panel was created by choosing the mapper-based FCR estimate closest to the simulated value per transcript. FCR was normalised to the maximum value across all timepoints. The data reconstructed from the read mapper alignments show increasing noise with decreasing mappability although some clear outliers are also visible in high mappability regions. Grey, dashed lines indicate 50% FCR. **B** Reconstructed half-lives per decay rate. The box-plots show a considerable number of outliers for both mappers; numbers of considered transcripts are plotted below the boxes. See main text for a discussion why reconstructed half-lives from simulated data are systematically higher than the true value (black boxes). **C-E** Correlations between estimated half-lives from simulated data and STAR, HISAT-3N and 'mosaic' data, respectively. Transcripts with >10% difference to simulated half-lives were considered outliers and are indicated by red triangles. Theoretical true half-lives per decay rate group are indicated by red dashed lines. **F** Upset plot showing numbers of outliers (including transcripts for which no half-life could be estimated) shared by mapper and mosaic data respectively. **G** Gene types of outliers (in one or both mappers), coloured by mappability (see Panel H for colour code). Most outliers were transcripts of protein coding genes. **H** Number of transcripts per mappability category for the analysed gene set.

Figure 3: FMAT reconstruction. **A** Median difference to simulated FMAT for unfiltered and intron-filtered data (shaded areas show interquartile ranges), negative values mean underestimation of simulated values. Intron filtering is described in the main text and improves results particularly for HISAT-3N in the low mappability segment. STAR shows larger underestimation with increasing conversion rates indicating difficulties to map spliced reads with more NCs. **B** Fractions of transcripts with different intron mappability categories, stratified by number of introns. Most transcripts with more than 3 introns contain introns from different mappability categories. **C** Median FMAT improvement increases with higher fractions of

filtered introns per transcript. HISAT-3N seems to profit more in the low mappability segment. **D** Distributions of simulated, mapper specific, intron-filtered and mosaic FMAT values for low mappability transcripts and 0 and 10% conversion rates. The dotted black line indicates the theoretical value of ⅓ (cf. Methods), numbers of observations are plotted below the boxes. Intron filtering and a 'mosaic' approach improve FMAT estimations and the 'mosaic' approach recovers data for more transcripts. A respective human metabolic labelling data plot is provided in Fig. S16 for comparison.

Figure 4: Effect of (NC) mappability on methylation site reconstruction. To estimate the impact of (NC) mapping biases on methylation site calling, we simulated RNA-BS-seq data for transcripts overlapping 4831 published mESC m^5C sites (see Supplement for details). **A** High correlation of published ('truth') and simulated methylation rates. **B** m^5C calls from HISAT-3N/meRanGs alignments were classified with respect to the simulated sites as TP/FP/FN. **C** FP and FN calls were predominantly located in regions with low mappability. **D** Methylation rate correlations for HISAT-3N and meRanGs. Note that these plots also contain methylation rates for FN (red) and FP (green) calls but shown correlation coefficients were calculated from TP calls only. Both mappers produced a significant number of FPs, several of them shared, as well as a few FN calls. Example calls are depicted in Fig. S18. **E** False calls were located predominantly in protein coding genes.

Figure 1

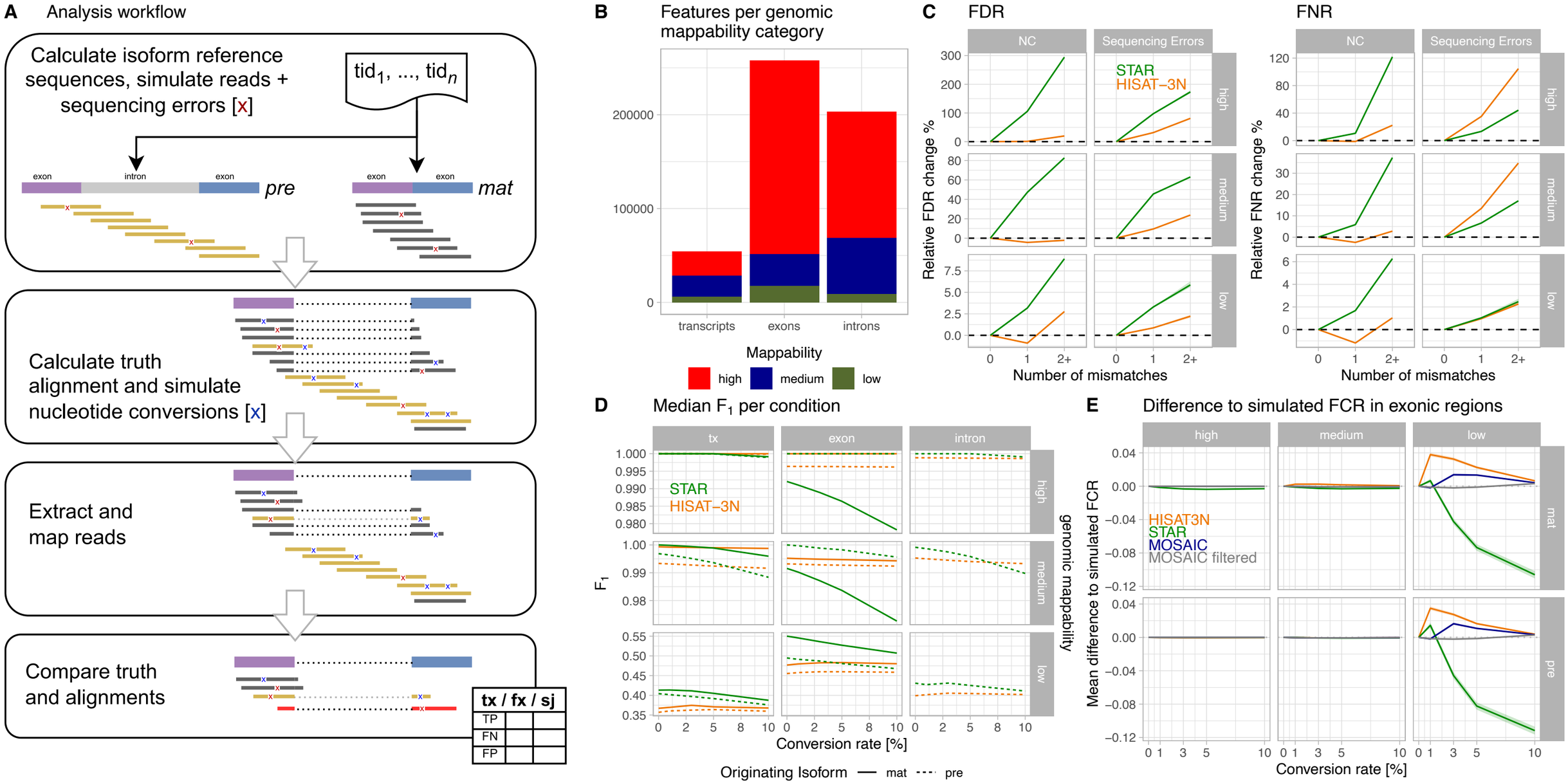
A
Analysis workflow
Calculate isoform reference sequences, simulate reads + sequencing errors [x]
tid1, ..., tidn
exon
intron
exon
pre
exon
exon
mat
Calculate truth alignment and simulate nucleotide conversions [x]
Extract and map reads
Compare truth and alignments
tx / fx / sj
TP
FN
FP
B
Features per genomic mappability category
200000
100000
0
transcripts
exons
introns
Mappability
high
medium
low
C
FDR
FNR
NC
Sequencing Errors
STAR
HISAT−3N
high
medium
low
Relative FDR change %
Relative FNR change %
Number of mismatches
D
Median F1 per condition
tx
exon
intron
STAR
HISAT−3N
F1
genomic mappability
Conversion rate [%]
Originating Isoform
mat
pre
E
Difference to simulated FCR in exonic regions
HISAT3N
STAR
MOSAIC
MOSAIC filtered
Mean difference to simulated FCR
Conversion rate [%]

Figure 2

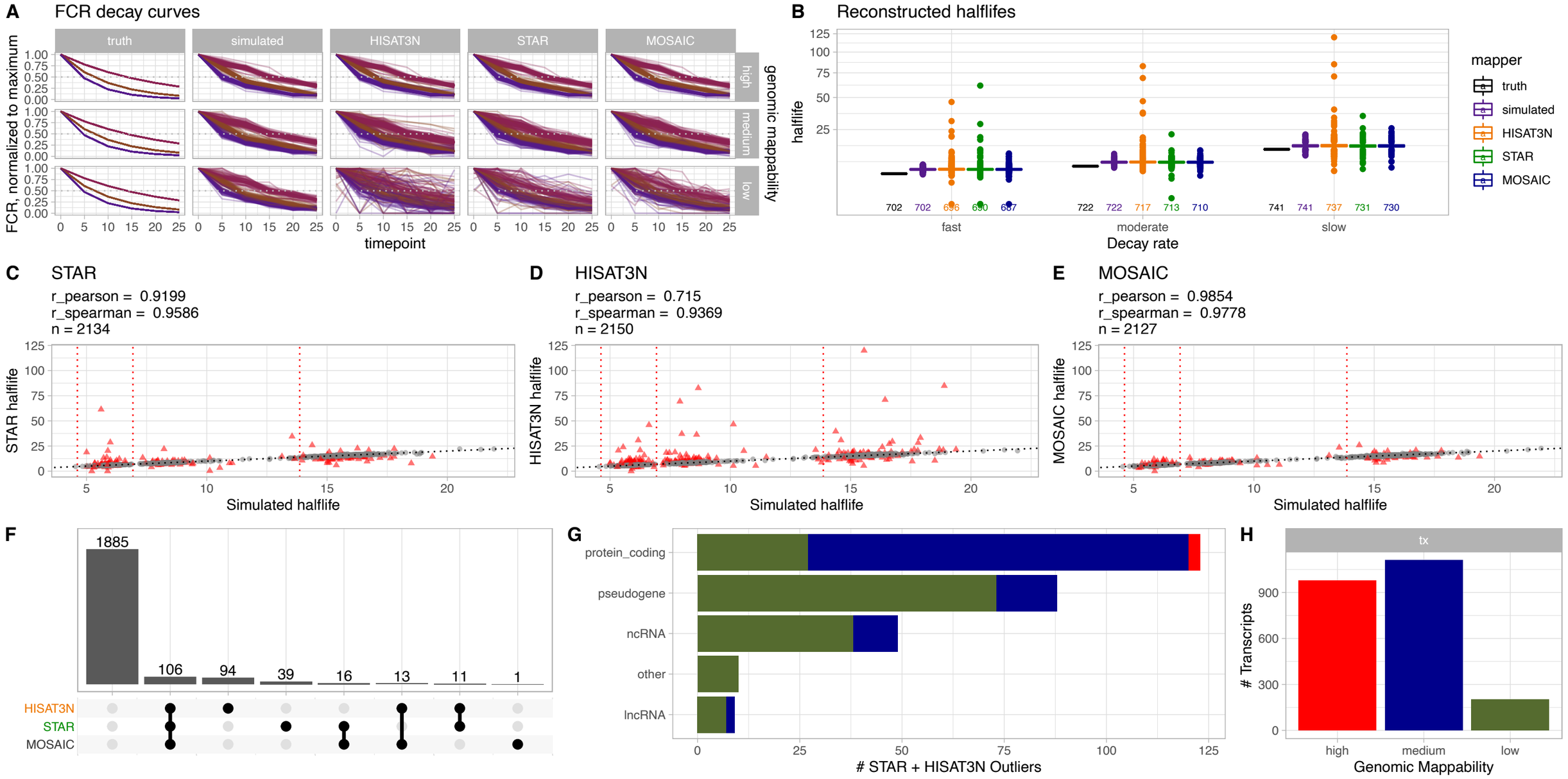
A
FCR decay curves
truth
simulated
HISAT3N
STAR
MOSAIC
high
medium
low
genomic mappability
FCR, normalized to maximum
timepoint
B
Reconstructed halflifes
halflife
mapper
truth
simulated
HISAT3N
STAR
MOSAIC
Decay rate
fast
moderate
slow
C
STAR
r_pearson = 0.9199
r_spearman = 0.9586
n = 2134
STAR halflife
Simulated halflife
D
HISAT3N
r_pearson = 0.715
r_spearman = 0.9369
n = 2150
HISAT3N halflife
Simulated halflife
E
MOSAIC
r_pearson = 0.9854
r_spearman = 0.9778
n = 2127
MOSAIC halflife
Simulated halflife
F
1885
106
94
39
16
13
11
1
HISAT3N
STAR
MOSAIC
G
protein_coding
pseudogene
ncRNA
other
lncRNA
STAR + HISAT3N Outliers
H
tx
Transcripts
high
medium
low
Genomic Mappability

Figure 3

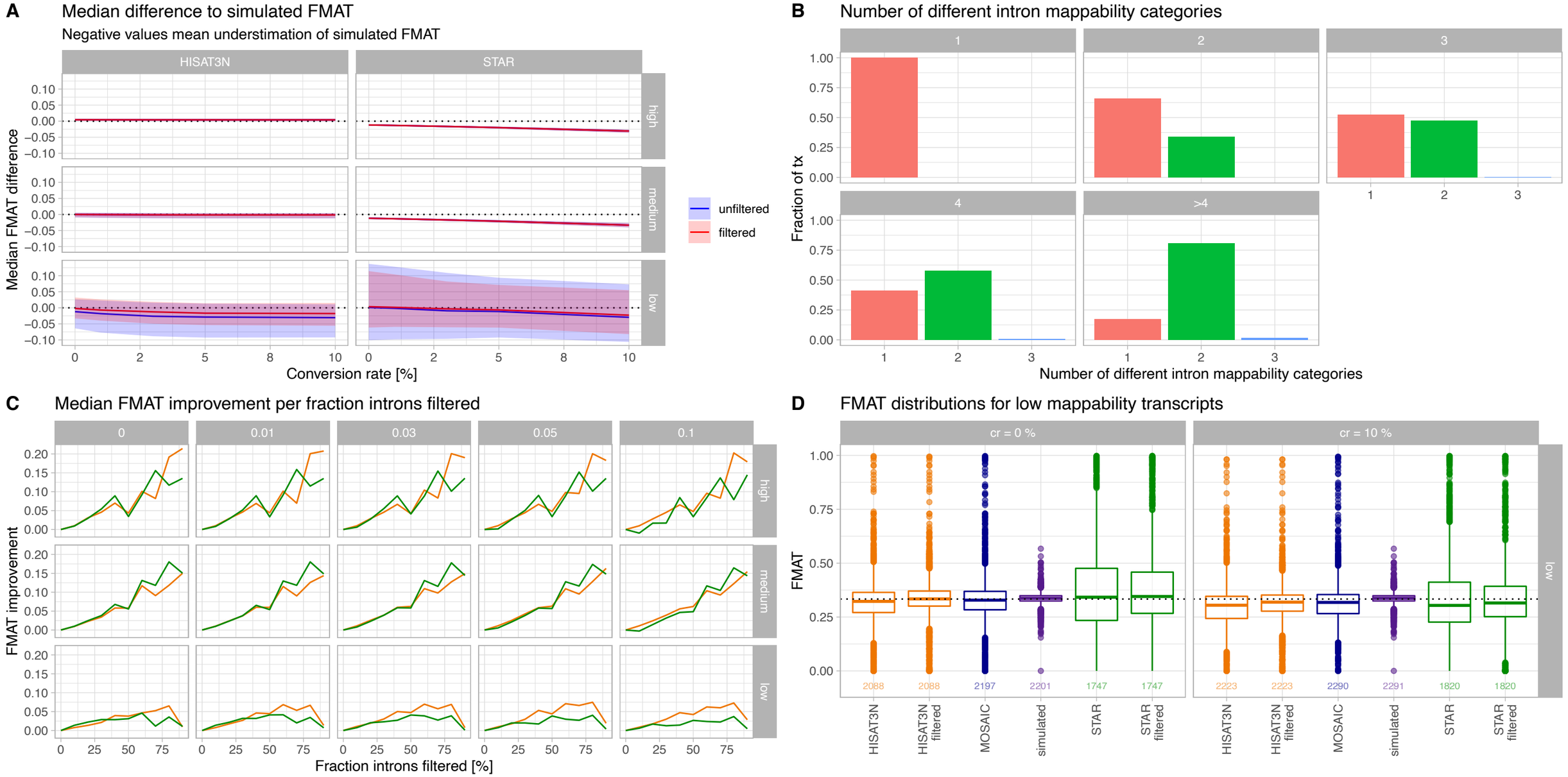
A
Median difference to simulated FMAT
Negative values mean understimation of simulated FMAT
HISAT3N
STAR
high
medium
low
Median FMAT difference
Conversion rate [%]
unfiltered
filtered
B
Number of different intron mappability categories
1
2
3
4
>4
Fraction of tx
Number of different intron mappability categories
C
Median FMAT improvement per fraction introns filtered
0
0.01
0.03
0.05
0.1
FMAT improvement
Fraction introns filtered [%]
D
FMAT distributions for low mappability transcripts
cr = 0 %
cr = 10 %
FMAT
2088
2088
2197
2201
1747
1747
2223
2223
2290
2291
1820
1820
HISAT3N
HISAT3N filtered
MOSAIC
simulated
STAR
STAR filtered

Figure 4

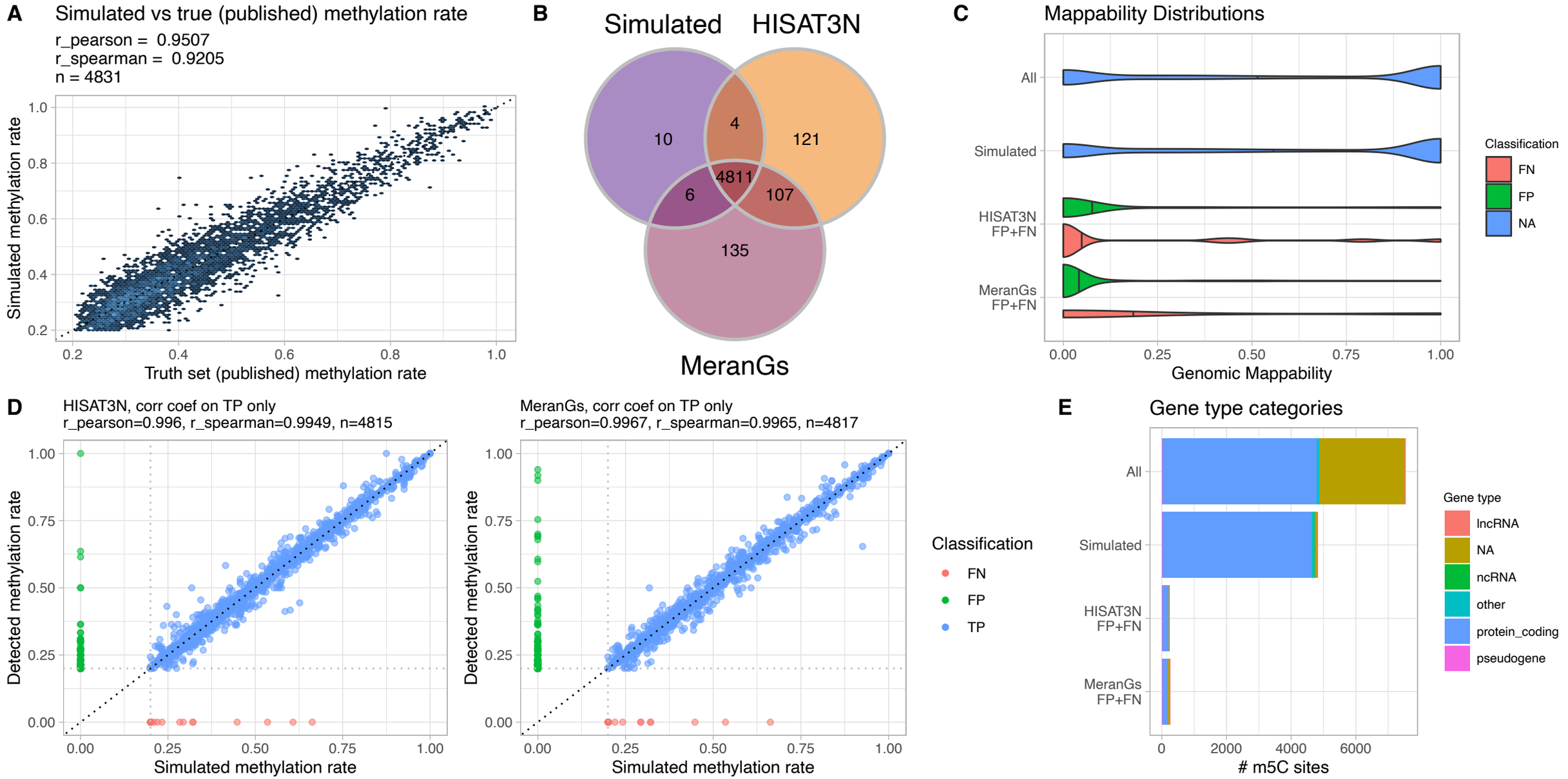
A
Simulated vs true (published) methylation rate
r_pearson = 0.9507
r_spearman = 0.9205
n = 4831
Simulated methylation rate
Truth set (published) methylation rate
B
Simulated
HISAT3N
MeranGs
10
4
121
4811
6
107
135
C
Mappability Distributions
All
Simulated
HISAT3N FP+FN
MeranGs FP+FN
Genomic Mappability
Classification
FN
FP
NA
D
HISAT3N, corr coef on TP only
r_pearson=0.996, r_spearman=0.9949, n=4815
MeranGs, corr coef on TP only
r_pearson=0.9967, r_spearman=0.9965, n=4817
Detected methylation rate
Simulated methylation rate
Classification
FN
FP
TP
E
Gene type categories
All
Simulated
HISAT3N FP+FN
MeranGs FP+FN
m5C sites
Gene type
lncRNA
NA
ncRNA
other
protein_coding
pseudogene